

Topology Optimization of Thermoelastic Structures using Stress-based Design Criteria

Joshua D. Deaton^{*} and Ramana V. Grandhi[†]
Wright State University, Dayton, OH, 45435

The design of thermal structures in the aerospace industry, including exhaust structures on embedded engine aircraft and hypersonic thermal protection systems, poses a number of complex design challenges that can be particularly well addressed using the material layout capabilities of structural topology optimization. However, no topology optimization methods are readily available with the necessary thermoelastic design capabilities as a significant portion of work in the topology optimization field is focused on cases of maximum stiffness design for structures subjected to externally applied mechanical loads. In addition, in the limited work on thermoelastic topology optimization, a direct treatment of thermal stresses, which are a primary consideration in thermal structures design, has not been demonstrated. Thus, in this paper, we present a method for the topology optimization of structures with combined mechanical and thermoelastic (temperature) loads that are subject to stress constraints. We present the necessary steps needed to address both the design-dependent thermal loads and accommodate the challenges of stress-based design criteria. A modern stress relaxation technique is utilized to remove the singularity phenomenon in stresses and the large number of constraints that result in the optimization problem are handled using a scaled aggregation technique that is shown to satisfy prescribed stress limits. Finally, the stress-based thermoelastic formulation is applied to two numerical example problems to demonstrate its effectiveness.

I. Introduction

The majority of work in structural topology optimization has focused on the minimum compliance (maximum stiffness) design of structures subjected to externally-applied, design-independent mechanical loading. This is likely a result of the simplicity of the structural optimization problem that arises, which due to the underlying mathematics of the problem, makes it comparatively straightforward to solve¹. However, there exists entire classes of problems that are not well addressed by this particular formulation². One of these instances is the topological design of structures subject to thermoelastic effects, which are a type of design-dependent load in topology optimization. In fact, due to the material layout capabilities of topology optimization, it holds great promise as a design tool for modern thermal structures applications in the aerospace industry. These include structural design for embedded engine aircraft exhaust structures and thermal protection systems for hypersonic flight vehicles^{3,4}.

Thermoelastic topology optimization was first investigated by Rodrigues and Fernandes, who used a homogenization method to minimize the compliance of structures with combined temperature and mechanical loading⁵. The problems investigated in their work have been frequently utilized as benchmark problems in many later publications. Li et al. utilized an evolutionary method for thermoelastic topology optimization for displacement minimization⁶ and problems with non-uniform temperature fields⁷. Kim et al.⁸ and Penmetsa et al.⁹ applied topology optimization to spacecraft thermal protection systems (TPS). Sigmund and Torquato used topology optimization to generate structures with extremal thermal expansion properties¹⁰ and Sigmund developed thermal micro-actuators with topology optimization^{11,12}. In addition, Jog incorporated nonlinear thermoelasticity¹³. Since these earlier works, thermoelastic topology optimization has been performed using density-based methods to investigate the best interpolation scheme for thermal loading¹⁴, the level set method¹⁵, and concurrent formulations to optimize both macro and micro-scale topology¹⁶. Recently, Pedersen and Pedersen questioned the application of the minimum compliance problem to thermoelasticity, which is used in a number of the early research works, because it cannot achieve good performance in minimizing deformation or strength for general problems in thermoelasticity. They proposed an alternative interpolation scheme in addition to a more suitable objective function based on uniform energy density, which was shown to produce superior results from a strength design point-of-view^{17,18}. The conclusion that compliance minimization is not suitable for thermoelastic problems is also supported in the work by Deaton and Grandhi, who demonstrate the inability of compliance minimization to find suitable solutions when thermal effects are significant in comparison to

^{*}Graduate Research Assistant, Department of Mechanical and Materials Engineering, AIAA Member.

[†]Distinguished Professor, Department of Mechanical and Materials Engineering, AIAA Fellow

mechanical loads. They circumvent this with alternative formulations based on fictitious mechanical loads to obtain desirable thermoelastic performance for these problems¹⁹. In another practical application, Wang et al. proposed a multi-objective optimization model to combine low thermal directional expansion with high structural stiffness²⁰. The recent prevalence of alternative formulations for thermoelastic topology optimization indicates that an increasing number of problems are not well addressed by purely compliance-based design. This is further driven by research that shows simple stiffening techniques cannot solve important problems that result from damaging thermal stresses³ and more advanced design techniques that more directly address thermal stresses are necessary.

As a result, we explore stress-based topology optimization, which may be more appropriate for thermoelasticity. Despite the fact that stresses are a primary consideration in any design problem, the topic has received little consideration in the literature compared to stiffness-based objectives until recently. This is due in large part to three primary challenges that make stress-based topological design more difficult than stiffness design. These are: (i) the singularity phenomenon, (ii) the local nature of stresses, and (iii) the highly nonlinear behavior of stress constraints²¹. Early work in the area was completed by Duysinx and Bendsøe²². More recently, Pereira et al.²³, Bruggi et al.^{24,25}, Guilherme and Fonseca²⁶, Le et al.²¹, París et al.^{27,28}, Lee et al.²⁹, Holmberg et al.³⁰, and others have explored various aspects of stress-based and stress-constrained topology optimization; however, to date no formulations that include thermal stresses have been developed.

In the following sections, a stress-based topology optimization capability that includes thermal stresses is introduced and demonstrated using numerical examples. Section II discusses the thermoelastic topology optimization formulation, including the finite element parameterization, interpolation schemes, and density filtering. Section III gives the techniques for stress-based design including singularity relaxation, an adaptive stress constraint technique, and adjoint sensitivity analysis for thermal stresses including design-dependent thermoelastic effects. Section IV provides the mathematical statement of the topology problems to be solved. Finally, Section V highlights the application of the formulation to numerical example problems followed by concluding remarks in Section VI.

II. Thermoelastic Topology Formulation

In this section, the framework of a density-based method^{1,31} for topology optimization, in which stress constraints are to be included, is discussed. Discussion includes incorporating the design-dependent thermoelastic effects in the finite element parameterization, selection of interpolation schemes, and density filtering.

A. Finite Element Parameterization

Figure 1 shows a generalized thermoelastic design domain Ω in two dimensions, which contains fixed displacement boundary conditions, externally applied surface tractions, and a prescribed temperature change (with respect to a reference temperature) that may be uniform or spatially varying. The domain consists of regions of fixed void material, fixed solid material (non-designable), and designable areas whose topology is to be determined from optimization.

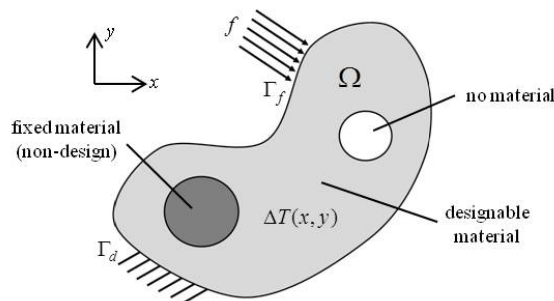


Figure 1. Generalized two-dimensional thermoelastic structural design domain.

The design domain is discretized using N finite elements with N_d designable and N_{nd} nondesign elements. Each designable element is assigned a density variable ρ_e ranging from $0 < \rho_{min} \leq \rho_e \leq 1$ with $e = 1, 2, \dots, N_d$ where densities of 0 and 1 indicate void and solid material, respectively. The density variables are collected in the density vector ρ . In addition to its density ρ_e , each designable finite element is assigned a design variable x_e , which also $0 \leq x_e \leq 1$ with $e = 1, 2, \dots, N_d$, and are stored in the design variable vector \mathbf{x} . The density variables become a function

of the design variables as $\rho_e(\mathbf{x})$ using the density filter discussed in Section II C.

Linear static equilibrium for a finite element representation of the domain, including both mechanical and temperature loading, is given by

$$\mathbf{K}(\boldsymbol{\rho})\mathbf{U}(\boldsymbol{\rho}) = \mathbf{F}(\boldsymbol{\rho}) \quad (1)$$

where $\mathbf{K}(\boldsymbol{\rho})$ is the global stiffness matrix, $\mathbf{U}(\boldsymbol{\rho})$ is the nodal displacement vector, and $\mathbf{F}(\boldsymbol{\rho})$ is the nodal load vector. In the general case of combined mechanical and thermoelastic load, \mathbf{F} consists of design-independent mechanical loading \mathbf{F}^m and design-dependent thermal loads $\mathbf{F}^{th}(\boldsymbol{\rho})$ as

$$\mathbf{F}(\boldsymbol{\rho}) = \mathbf{F}^m + \mathbf{F}^{th}(\boldsymbol{\rho}). \quad (2)$$

By taking the thermal load vector as a function of the density variables, the appropriate dependency of thermal loading on the design configuration is captured. The stiffness matrix $\mathbf{K}(\boldsymbol{\rho})$ is assembled as the summation of element stiffnesses by

$$\mathbf{K}(\boldsymbol{\rho}) = \sum_{e=1}^{N_d} \mathbf{k}_e(\rho_e) \quad (3)$$

where

$$\mathbf{k}_e(\rho_e) = \int_{\Omega_e} \mathbf{B}_e^T \mathbf{C}_e(\rho_e) \mathbf{B}_e d\Omega. \quad (4)$$

Here, \mathbf{B}_e is the element strain-displacement matrix, which consists of derivatives of the element shape functions that are independent of topology design variables. \mathbf{C}_e is the element elasticity matrix, which for isotropic materials can be written as a linear function of elastic modulus as

$$\mathbf{C}_e(\rho_e) = E(\rho_e) \bar{\mathbf{C}}_e \quad (5)$$

where $\bar{\mathbf{C}}_e$ consists of constant terms related to the material constitutive matrix and $E(\rho_e)$ is the elastic modulus of element e and is dependent on density variables. For nondesign elements, the previous equations can be utilized by simply assuming $\rho_e = 1$. The mechanical load vector \mathbf{F}^m is assembled from externally applied forces on specific degrees of freedom. The thermal load vector $\mathbf{F}^{th}(\boldsymbol{\rho})$ is parameterized using the thermal stress coefficient (TSC)^{5,14} for topology optimization and described as follows.

The nodal load vector for a designable element e is given as

$$\mathbf{f}_e^{th}(\rho_e) = \int_{\Omega_e} \mathbf{B}_e^T \mathbf{C}_e(\rho_e) \boldsymbol{\epsilon}_e^{th}(\rho_e) d\Omega \quad (6)$$

where $\boldsymbol{\epsilon}_e^{th}(\rho_e)$ is the thermal strain vector for the element

$$\boldsymbol{\epsilon}_e^{th}(\rho_e) = \alpha(\rho_e) \Delta T_e \boldsymbol{\phi}^T. \quad (7)$$

Here, $\alpha(\rho_e)$ is the thermal expansion coefficient that is also dependent on element density, ΔT_e is the temperature change of element e (taken here as the average of nodal temperatures), and $\boldsymbol{\phi}$ is simply the vector [1 1 0] for two dimensional problems with isotropic materials. Substitution of Equations (5) and (7) into (6) yields

$$\mathbf{f}_e^{th}(\rho_e) = E(\rho_e) \alpha(\rho_e) \int_{\Omega_e} \mathbf{B}_e^T \bar{\mathbf{C}}_e \Delta T_e \boldsymbol{\phi}^T d\Omega \quad (8)$$

in which we note that both $E(\rho_e)$ and $\alpha(\rho_e)$ are dependent on density variables and thus both necessitate material interpolation. To simplify, we combine these parameters into a single thermal load coefficient as

$$\beta(\rho_e) = E(\rho_e) \alpha(\rho_e). \quad (9)$$

This quantity is then treated as an inherent material property and $\mathbf{f}_e^{th}(\rho_e)$ can be rewritten as

$$\mathbf{f}_e^{th}(\rho_e) = \beta(\rho_e) \int_{\Omega_e} \mathbf{B}_e^T \bar{\mathbf{C}}_e \Delta T_e \boldsymbol{\phi}^T d\Omega. \quad (10)$$

Finally, the global thermal load vector is assembled by summing element contributions

$$\mathbf{F}^{th}(\boldsymbol{\rho}) = \sum_{e=1}^N \mathbf{f}_e^{th}(\rho_e). \quad (11)$$

Again, the element thermal load vector for nondesign elements can be obtained from the previous relations by taking $\rho_e = 1$.

After solving Equation (1) to determine the displacements, the stress tensor for each element is computed as a post processing step by

$$\boldsymbol{\sigma}_e = E_o \bar{\mathbf{C}}_e \mathbf{B}_e \mathbf{U}_e - E_o \bar{\mathbf{C}}_e \alpha_o \boldsymbol{\phi}^T \Delta T_e, \quad (12)$$

which we note is only implicitly dependent on the topology and thus is called the solid stress vector. For a two-dimensional continuum element, the stress vector contains two normal stress components, $\sigma_{x,e}$ and $\sigma_{y,e}$, in addition to a shear stress $\tau_{xy,e}$ as

$$\boldsymbol{\sigma}_e = \begin{bmatrix} \sigma_{x,e} & \sigma_{y,e} & \tau_{xy,e} \end{bmatrix}^T. \quad (13)$$

The principal stresses and maximum shear stress in element e can be computed as

$$\sigma_{1,e} = \frac{\sigma_{x,e} + \sigma_{y,e}}{2} + \sqrt{\left(\frac{\sigma_{x,e} - \sigma_{y,e}}{2}\right)^2 + \tau_{xy,e}^2}, \quad (14)$$

$$\sigma_{2,e} = \frac{\sigma_{x,e} + \sigma_{y,e}}{2} - \sqrt{\left(\frac{\sigma_{x,e} - \sigma_{y,e}}{2}\right)^2 + \tau_{xy,e}^2}, \quad (15)$$

$$\tau_{max,e} = \sqrt{\left(\frac{\sigma_{x,e} - \sigma_{y,e}}{2}\right)^2 + \tau_{xy,e}^2}, \quad (16)$$

which yield the most severe (max/min) normal and shear stress conditions in element e for the prescribed stress vector. While failure in an element can be based on the principal or maximum shear stresses, in design various failure metrics are commonly utilized to generalize material failure to states of combined normal (tension and compression) and shear stress. At this point, we assume that a generalized stress failure criterion $F_e^{(g)}$ for element e can be computed as a function of the elements in the solid stress tensor as

$$F_e^{(g)} = F_e^{(g)}(\boldsymbol{\sigma}_e). \quad (17)$$

In this work, the common von Mises failure criteria is utilized and is given as

$$\sigma_{vm,e} = \sqrt{\sigma_{x,e}^2 - \sigma_{x,e}\sigma_{y,e} + \sigma_{y,e}^2 + 3\tau_{xy,e}^2}. \quad (18)$$

B. Interpolation Schemes

It is known that in the presence of design-dependent loading, which includes thermal loads, the usual SIMP (Solid Isotropic Material with Penalization) interpolation scheme presents numerical difficulties due in large part to the fact that its sensitivity vanishes with small density values. As a result, in the presence of thermal loads, the RAMP (Rational Approximation of Material Properties) model is adopted. Thus, the stiffness and thermal load are interpolated according to

$$E(\rho_e) = \eta_E(\rho_e)E_o = \frac{\rho_e}{1 + R_E(1 - \rho_e)}E_o \quad (19)$$

$$\beta(\rho_e) = \eta_\beta(\rho_e)E_o\alpha_o = \frac{\rho_e}{1 + R_\beta(1 - \rho_e)}E_o\alpha_o \quad (20)$$

where R_E and R_β are RAMP penalization parameters. In addition, E_o and α_o are baseline material properties for the elastic modulus and coefficient of thermal expansion, respectively. For comparison on a room temperature example, we note here the SIMP interpolation on stiffness takes the usual power law form

$$E(\rho_e) = \rho_e^{p_E} E_o \quad (21)$$

where p_E is the SIMP penalization parameter on the elastic modulus.

C. Density Filtering

In order to prevent checker-boarding and enforce length scale we use the density filter³² given by Equation (22)

$$\rho_e = \frac{1}{\sum_{i \in N_e} H_{ei}} \sum_{i \in N_e} H_{ei} x_i \quad (22)$$

where ρ_e is the physical density of element e , N_e is the set of elements i for which the center-to-center distance $\Delta(e, i)$ to element e is smaller than the filter radius r_{min} , and H_{ei} is a weight factor given by

$$H_{ei} = \max(0, r_{min} - \Delta(e, i)). \quad (23)$$

Here we note the difference between the design variable x and the physical density ρ . The finite element model is parameterized using the density variables contained in ρ , which are now computed by applying the density filter to the design variables x upon which the optimizer operates. This is important when computing sensitivity information in the optimization, which must be obtained with respect to the design variable x . In implementation, the sensitivity of a response f is obtained with respect to the physical densities $\partial f / \partial \rho_e$ using the adjoint sensitivity method. Thus, the following chain rule must be applied to obtain the sensitivity with respect to a design variable x_j

$$\frac{\partial f}{\partial x_j} = \sum_{e \in N_j} \frac{\partial f}{\partial \rho_e} \frac{\partial \rho_e}{\partial x_j} = \sum_{e \in N_j} \frac{1}{\sum_{i \in N_e} H_{ei}} H_{je} \frac{\partial f}{\partial \rho_e}. \quad (24)$$

III. Methods for Stress-based Criteria

In this section, the special techniques required to address the challenges of incorporating stress constraints in topology optimization are introduced. These challenges include the singularity phenomena in the elemental stress function and the need to efficiently treat the local nature of stress constraints.

A. Relaxed Stress

In this work, the relaxation method of Le et al.²¹ is adopted to relax elemental stress values and remove the singularity phenomena. This technique works by applying an interpolation on the element failure criteria as defined by Equation (17) according to

$$F_e^{(r)} = \eta_F(\rho_e) F_e^{(g)} \quad (25)$$

where $F_e^{(r)}$ is the relaxed failure criterion and $\eta_F(\rho_e) = \rho_e^{1/2}$ in this work. Since this method was developed for stresses of mechanical origin, the following numerical exercise is provided to demonstrate its effectiveness for stresses due to mechanical, thermal, and combined thermal/mechanical loading. The simple finite element model for the study is shown in Figure 2. It is constructed using using 2D four-node elements in plane stress and the material properties of the structure are taken as $E = 70$ GPa, $\nu = 0.3$, $\alpha = 25 \times 10^{-6}$ 1/°C, and the thickness is taken as $t = 1$ cm. The model is analyzed using four different loading cases and boundary conditions, which subject it to various cases of mechanical (2a and 2b), thermal (2c), and (2d) combined stresses.

Figure 3 gives the von Mises stress in element 1 as a function of its density. In the figure, the dashed lines show the solid stress computed directly from Equation (18). The singularity phenomena is readily evident in the solid stress, which increases significantly as the density in element 1 is reduced. However, when the relaxation is applied to the solid stress according to Equation (25), where the generalized failure criterion has been replaced with the von Mises stress, we observe that the singularity in the stress is arrested as density is decreased. Moreover, as the density nears zero, which corresponds to no material, a state of zero stress is achieved. This is realized for all cases of mechanical, thermal, and combined stress states. In addition, a penalizing effect in terms of stress is observed for intermediate densities. That is, intermediate density material experiences a more severe stress state than both solid and void material, which is desirable in the formulation of the topology optimization to ensure that the non-physical intermediate density is removed in the final design.

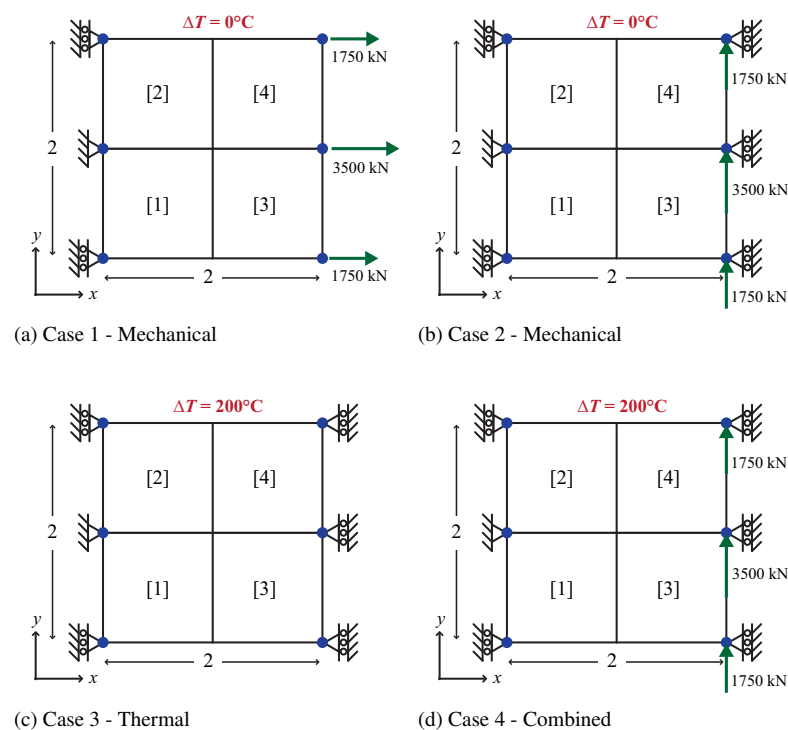


Figure 2. Model, boundary conditions, and load cases for the validation of the relaxed stress technique. Note dimensions shown in meters. (a,b) Mechanical loading, (c) Thermal Loading, and (d) Combined Loading.

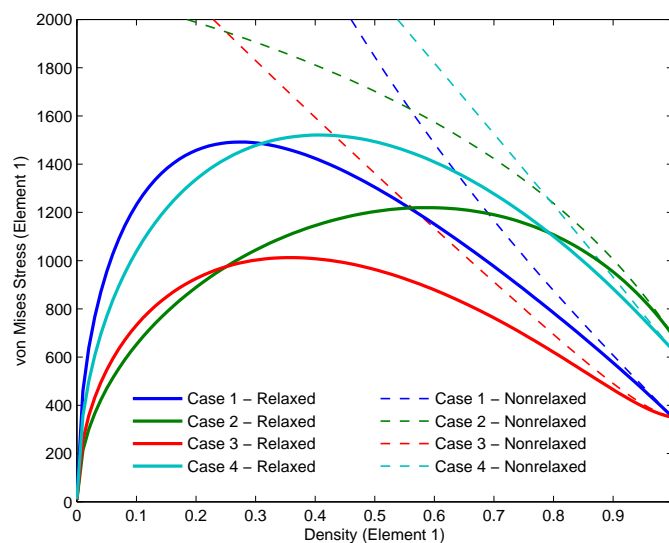


Figure 3. Validation of stress relaxation - stress (von Mises) in element 1 plotted as a function of element 1 density.

B. Scaled Stress Aggregation

Another primary challenge in stress-based topology optimization is effectively capturing the maximum stress at a level of computational expense that is suitable for industrial size topology optimization problems. Since it is computationally impossible to place stress constraints on every element, a modified p -norm function is utilized to aggregate the failure criterion value of many elements into a manageable number of constraints. If the elements in the model are split into n groups, the p -norm function for group m is given by

$$\text{PN}_m = \left[\sum_{e=1}^{N_m} \left(\frac{F_e^{(r)}}{\bar{F}} \right)^p \right]^{1/p} \quad (26)$$

where N_m is the number of elements in group m , p is a tuning parameter, and \bar{F} is the limit value on the failure criterion $F_e^{(r)}$. In general, higher values of p increase the accuracy of the aggregation with $\text{PN}_m \rightarrow \max(F_e^{(r)}/\bar{F})_m$ (the maximum value of the normalized failure criterion in group m) for $p \rightarrow \infty$; however, in practice both numerical and optimization convergence issues occur if the value selected for p is too large. In the optimization literature, when using p -norm functions, suitable values for p are generally found in the range from 4 to 10. This limitation on the values of p ensures that considerable error between PN_m and $\max(F_e^{(r)}/\bar{F})_m$ is present and we cannot reliably enforce the limit value \bar{F} . To remedy this, a scaling technique is employed to gradually scale the PN_m towards $\max(F_e^{(r)}/\bar{F})_m$ over the course of the iterative optimization process.

If no discrepancy exists between PN_m and $\max(F_e^{(r)}/\bar{F})_m$, material failure is predicted if $\text{PN}_m \geq 1$ and a constraint in the optimization problem can be posed as

$$g_m = \text{PN}_m - 1 \leq 0. \quad (27)$$

If used in a typical gradient-based optimization process, as convergence is reached the value of PN_m would converge as well. When considering the inherent discrepancy between PN_m and $\max(F_e^{(r)}/\bar{F})_m$, the difference approaches a constant value. Exploiting this behavior, the constraint in Equation (27) can be rewritten with an adaptive scaling factor s_m^i as

$$g_m = s_m^i \text{PN}_m^i - 1 \leq 0. \quad (28)$$

where i indicates the iteration number and s_m^i is the ratio between PN_m and $\max(F_e/\bar{\sigma})$ in group m in the previous iteration. This is simply calculated as

$$s_m^i = \frac{\text{PN}_m^{i-1}}{\max(F_e^{(r)}/\bar{F})_m^{i-1}} \quad (29)$$

using stored information. We note that the scaling ratio s_m^i is a non-continuous quantity; however, since it approaches a constant value as the optimization progresses, convergence is not impeded so long as excessive step sizes are not permitted.

C. Sensitivity Analysis

In the sensitivity analysis implementation, care should be taken to properly treat the stress in elements that are designable (dependent on density) compared to elements that remain solid. In the derivation that follows, this consideration is noted where appropriate.

We begin by differentiating Equation (28) (note that the superscript i that gives the iteration number has been removed for clearer presentation) with respect to a density variable ρ_j

$$\frac{dg_m}{d\rho_j} = s_m \frac{d\text{PN}_m}{d\rho_j}. \quad (30)$$

The derivative of the aggregation function PN_m with respect to the density variable is

$$\frac{d\text{PN}_m}{d\rho_j} = \sum_{e=1}^{N_m} \frac{\partial \text{PN}_m}{\partial F_e^{(r)}} \frac{dF_e^{(r)}}{d\rho_j} \quad (31)$$

In Equation (31) the first partial derivative term $\partial \text{PN}_m / \partial F_e^{(r)}$ is obtained by differentiating Equation (26) with respect to the relaxed elemental failure criterion $F_e^{(r)}$, which yields

$$\frac{\partial \text{PN}_m}{\partial F_e^{(r)}} = \left[\sum_{e=1}^{N_m} \left(\frac{F_e^{(r)}(\rho_e)}{\bar{F}} \right)^p \right]^{(1/p-1)} \left(\frac{F_e^{(r)}(\rho_e)}{\bar{F}} \right)^{p-1}. \quad (32)$$

Next we recall that $F_e^{(r)}$ is the product of the stress interpolation η_F and, in the most general case, the solid element failure criterion $F_e^{(g)}$ as given in Equation (25). Differentiating this relation yields

$$\begin{aligned} \frac{dF_e^{(r)}}{d\rho_j} &= \frac{\partial F_e^{(r)}}{\partial \eta_F} \frac{d\eta_F}{d\rho_j} + \left(\frac{\partial F_e^{(r)}}{\partial F_e^{(g)}} \right) \left(\frac{\partial F_e^{(g)}}{\partial \sigma_e} \right)^T \frac{d\sigma_e}{d\rho_j} \\ &= F_e^{(g)} \frac{d\eta_F}{d\rho_j} + \eta_F(\rho_e) \left(\frac{\partial F_e^{(g)}}{\partial \sigma_e} \right)^T \frac{d\sigma_e}{d\rho_j} \end{aligned} \quad (33)$$

where the term $d\sigma_e/d\rho_j$ is the derivative of the solid stress tensor of element e with respect to the density variable. This is computed by differentiating Equation (12), which gives

$$\frac{d\sigma_e}{d\rho_j} = \bar{\mathbf{C}}_e \mathbf{B}_e \frac{d\mathbf{U}_e}{d\rho_j} = \bar{\mathbf{C}}_e \mathbf{B}_e \left(\frac{\partial \mathbf{U}_e}{\partial \mathbf{U}} \right)^T \frac{d\mathbf{U}}{d\rho_j} \quad (34)$$

where $\partial \mathbf{U}_e / \partial \mathbf{U}$ forms a transformation from local element degrees of freedom to the global degrees of freedom. Substituting Equation (34) into (33) and (33) into (31) yields

$$\begin{aligned} \frac{d\text{PN}_m}{d\rho_j} &= \sum_{e=1}^{N_m} \left[\frac{\partial \text{PN}}{\partial F_e^{(r)}} \left(F_e^{(g)} \frac{d\eta_F}{d\rho_j} + \eta_F(\rho_e) \left(\frac{\partial F_e^{(g)}}{\partial \sigma_e} \right)^T \bar{\mathbf{C}}_e \mathbf{B}_e \left(\frac{\partial \mathbf{U}_e}{\partial \mathbf{U}} \right)^T \frac{d\mathbf{U}}{d\rho_j} \right) \right] \\ &= \sum_{e=1}^{N_m} \left[\frac{\partial \text{PN}}{\partial F_e^{(r)}} F_e^{(g)} \frac{d\eta_F}{d\rho_j} \right] \\ &\quad + \sum_{e=1}^{N_m} \left[\frac{\partial \text{PN}}{\partial F_e^{(r)}} \eta_F(\rho_e) \left(\frac{\partial F_e^{(g)}}{\partial \sigma_e} \right)^T \bar{\mathbf{C}}_e \mathbf{B}_e \left(\frac{\partial \mathbf{U}_e}{\partial \mathbf{U}} \right)^T \right] \frac{d\mathbf{U}}{d\rho_j}. \end{aligned} \quad (35)$$

We note that the $d\eta_F/d\rho_j$ term in the first summation in Equation (35) is nonzero only for $e = j$. Thus, the summation can be ignored and the equation can be reduced to

$$\frac{d\text{PN}_m}{d\rho_j} = \frac{\partial \text{PN}}{\partial F_j^{(r)}} F_j^{(g)} \frac{d\eta_F}{d\rho_j} + \sum_{e=1}^{N_m} \left[\frac{\partial \text{PN}}{\partial F_e^{(r)}} \eta_F(\rho_e) \left(\frac{\partial F_e^{(g)}}{\partial \sigma_e} \right)^T \bar{\mathbf{C}}_e \mathbf{B}_e \left(\frac{\partial \mathbf{U}_e}{\partial \mathbf{U}} \right)^T \right] \frac{d\mathbf{U}}{d\rho_j}. \quad (36)$$

Differentiating Equation (1) with respect to ρ_j and rearranging gives

$$\frac{d\mathbf{U}}{d\rho_j} = \mathbf{K}^{-1} \left(\frac{d\mathbf{F}^{th}}{d\rho_j} - \frac{d\mathbf{K}}{d\rho_j} \mathbf{U} \right). \quad (37)$$

Substituting the preceding relation into Equation (36) and introducing the adjoint variable λ yields

$$\frac{d\text{PN}_m}{d\rho_j} = \frac{\partial \text{PN}}{\partial F_j^{(r)}} F_j^{(g)} \frac{d\eta_F}{d\rho_j} + \lambda^T \left(\frac{d\mathbf{F}^{th}}{d\rho_j} - \frac{d\mathbf{K}}{d\rho_j} \mathbf{U} \right) \quad (38)$$

where the adjoint variable is determined by the solution of the adjoint problem

$$\mathbf{K} \lambda = \sum_{e=1}^{N_m} \left[\frac{\partial \text{PN}}{\partial F_e^{(r)}} \eta_F(\rho_e) \frac{\partial F_e^{(g)}}{\partial \sigma_e} (\bar{\mathbf{C}}_e \mathbf{B}_e)^T \frac{\partial \mathbf{U}_e}{\partial \mathbf{U}} \right]. \quad (39)$$

Note that Equations (38) and (39) give the sensitivity using a general stress failure criteria. The term $\partial F_e^{(g)}/\partial \sigma_e$ varies according to how the selected failure criteria is calculated using the components of the element stress tensor. The sensitivity using the von Mises failure criterion is determined by differentiating Equation (18) with respect to the elements of the stress tensor as

$$\frac{\partial F_e^{(vm)}}{\partial \sigma_e} = \left\{ \begin{array}{c} \frac{\partial F_e^{(vm)}}{\partial \sigma_{x,e}} \\ \frac{\partial F_e^{(vm)}}{\partial \sigma_{y,e}} \\ \frac{\partial F_e^{(vm)}}{\partial \tau_{xy,e}} \end{array} \right\} \quad (40)$$

where

$$\frac{\partial F_e^{(vm)}}{\partial \sigma_{x,e}} = \frac{1}{2F_e^{(vm)}} (2\sigma_{x,e} - \sigma_{y,e}), \quad (41)$$

$$\frac{\partial F_e^{(vm)}}{\partial \sigma_{y,e}} = \frac{1}{2F_e^{(vm)}} (2\sigma_{y,e} - \sigma_{x,e}), \quad (42)$$

$$\frac{\partial F_e^{(vm)}}{\partial \tau_{xy,e}} = \frac{3\tau_{xy,e}}{F_e^{(vm)}}. \quad (43)$$

1. Validation

Using the models and analysis cases previously given in Figure 2, the analytical sensitivity analysis formulation for the aggregated measure given by Equations (31) to (43) is validated against finite difference sensitivities. The sensitivity of the aggregated measure over various regions with respect to the density of element 1 is found. For each region described in Table 1 (note some regions contain only a single element), the aggregated measure is computed according to Equation (26) using the von Mises failure criterion and $\bar{\sigma} = 350$ MPa. We note that by testing these regions, multiple cases including designable elements, nondesign elements, and regions of mixed elements are evaluated.

Table 1. Region definitions for sensitivity analysis validation of the aggregated stress measure.

Region Number	Elements
1	1
2	2
3	1 and 2
4	1 to 4

The sensitivity of the aggregated measures are shown in Figures 4a to 4d. In each plot, different loading and boundary conditions are indicated by different colors with the analytical sensitivity given by solid lines and finite difference validation points indicated by filled dots. Finally, the variation of the sensitivity with respect to the density of element 1 is plotted (with the density along the horizontal axis) to demonstrate the nonlinear dependence of the stress sensitivities on density. From all the plots in Figure 4 it is observed that the finite difference points lie exactly on the analytical sensitivity curves, which indicates the accuracy of adjoint formulation.

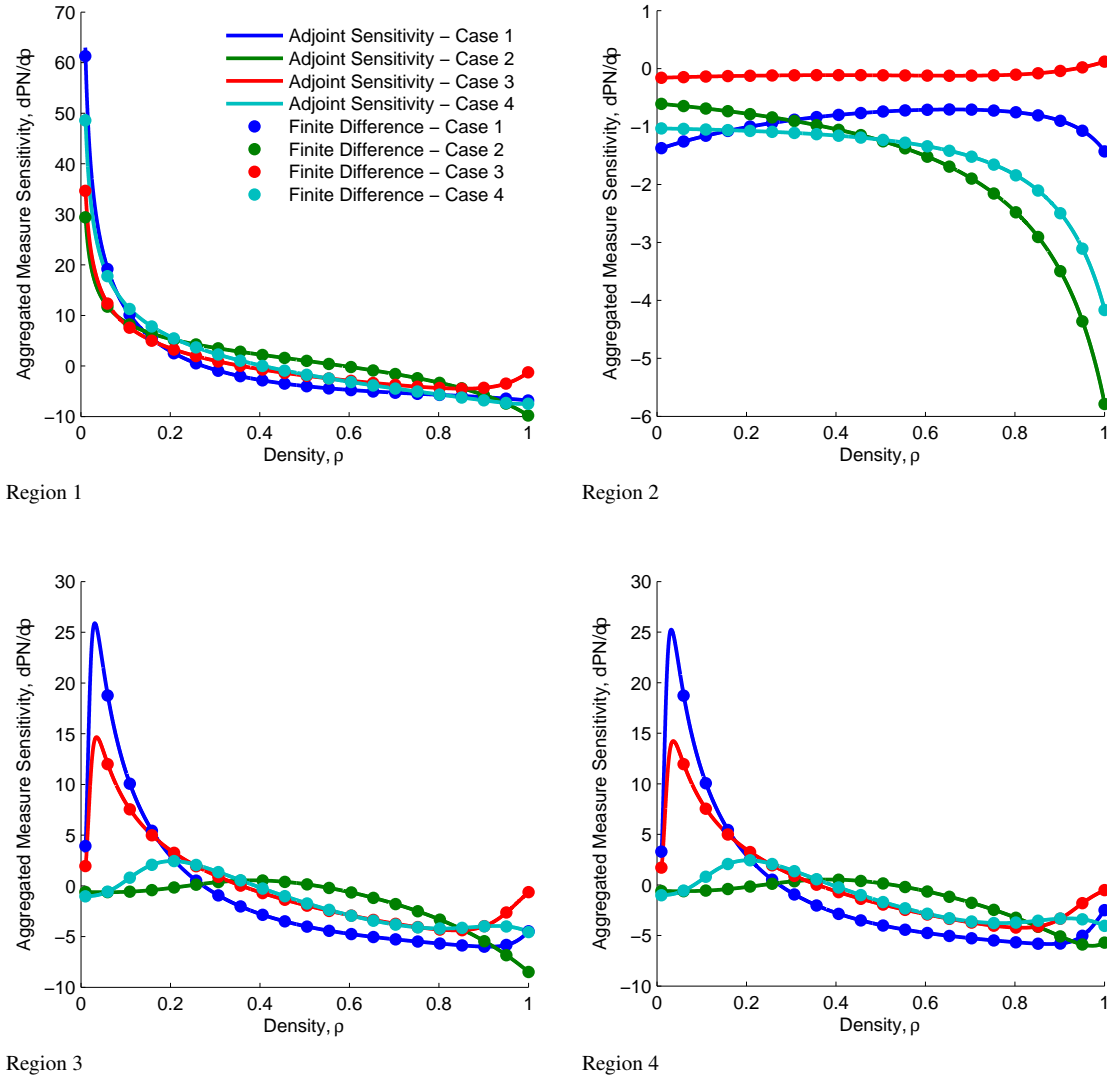


Figure 4. Validation of analytical sensitivity analysis for the aggregated stress measure with multiple region definitions indicated by color and multiple loading and boundary conditions from Figure 2.

D. Element Grouping

Rather than a single global aggregation, multiple constraints of the form in Equation (28) are utilized with each acting over a group of elements. Elements are grouped according to their stress-level by computing the element stress failure criterion and sorting the values in descending order. For N elements sorted into n groups this can be done as

$$\underbrace{F_1^{(g)} \geq F_2^{(g)} \geq F_3^{(g)} \geq \dots \geq F_{\frac{N}{N_m}}^{(g)}}_{\text{region 1}} \geq \dots \geq \underbrace{F_{\frac{2N}{N_m}}^{(g)}}_{\text{region 2}} \geq \dots \geq \underbrace{F_{\frac{(n-1)N}{N_m}}^{(g)}}_{\text{region } n-1} \geq \dots \geq \underbrace{F_N^{(g)}}_{\text{region } n} \quad (44)$$

where the first $n-1$ clusters contain N_m elements and the last cluster holds the remaining elements. Note that alternative grouping techniques, along with the resorting of elements during the optimization process, have been explored in the literature³⁰ and may hold computational advantages in some problems; however, in this work we sort elements at only the first iteration and maintain the same grouping throughout the optimization.

IV. Optimization Problem Statements

Using the finite element parameterization and additional techniques above, a number of different topology optimization problems can be formulated. The mathematical statement for a generalized topology optimization problem is given by

$$\begin{aligned}
 \min : & \quad f(\boldsymbol{\rho}, \mathbf{U}(\boldsymbol{\rho})) \\
 \text{subject to :} & \quad \mathbf{K}(\boldsymbol{\rho})\mathbf{U}(\boldsymbol{\rho}) = \mathbf{F}^m + \mathbf{F}^{th}(\boldsymbol{\rho}) \\
 & \quad g_i(\boldsymbol{\rho}, \mathbf{U}(\boldsymbol{\rho})) \leq 0 \\
 \text{variables :} & \quad 0 < x_e \leq 1 \text{ for } e = 1, 2, \dots, N
 \end{aligned} \tag{45}$$

where f is the objective function and g_i is the set of constraints. Using this form, the common minimum compliance (maximum stiffness), material constrained problem is stated as

$$\begin{aligned}
 \min : & \quad c(\boldsymbol{\rho}) = \mathbf{U}(\boldsymbol{\rho})^T \mathbf{K}(\boldsymbol{\rho}) \mathbf{U}(\boldsymbol{\rho}) \\
 \text{subject to :} & \quad \mathbf{K}(\boldsymbol{\rho})\mathbf{U}(\boldsymbol{\rho}) = \mathbf{F}^m + \mathbf{F}^{th}(\boldsymbol{\rho}) \\
 & \quad g_1(\boldsymbol{\rho}) = \sum_{e=1}^{N_d} (\rho_e v_e - V_f v_e) \leq 0 \\
 \text{variables :} & \quad 0 < x_{min} \leq x_e \leq 1 \text{ for } e = 1, 2, \dots, N_d
 \end{aligned} \tag{46}$$

where v_e is the elemental volume and V_f is the allowable volume fraction. The minimum material, stress-constrained problem is given by

$$\begin{aligned}
 \min : & \quad f(\boldsymbol{\rho}) = \sum_{e=1}^{N_d} (\rho_e v_e) \\
 \text{subject to :} & \quad \mathbf{K}(\boldsymbol{\rho})\mathbf{U}(\boldsymbol{\rho}) = \mathbf{F}^m + \mathbf{F}^{th}(\boldsymbol{\rho}) \\
 & \quad g_m(\boldsymbol{\rho}, \mathbf{U}) = s_m^i \text{PN}(\boldsymbol{\rho}, \mathbf{U})_m^i - 1 \leq 0 \text{ for } m = 1, 2, \dots, n \\
 \text{variables :} & \quad 0 < x_{min} \leq x_e \leq 1 \text{ for } e = 1, 2, \dots, N_d
 \end{aligned} \tag{47}$$

where a total of n aggregated constraints on stress failure are utilized. Finally, a minimum compliance problem with material usage and stress constraints is useful in the design of high stiffness structures that also satisfy stress limits. Such a problem can be stated as

$$\begin{aligned}
 \min : & \quad c(\boldsymbol{\rho}) = \mathbf{U}(\boldsymbol{\rho})^T \mathbf{K}(\boldsymbol{\rho}) \mathbf{U}(\boldsymbol{\rho}) \\
 \text{subject to :} & \quad \mathbf{K}(\boldsymbol{\rho})\mathbf{U}(\boldsymbol{\rho}) = \mathbf{F}^m + \mathbf{F}^{th}(\boldsymbol{\rho}) \\
 & \quad g_1(\boldsymbol{\rho}) = \sum_{e=1}^{N_d} (\rho_e v_e - V_f v_e) \leq 0 \\
 & \quad g_m(\boldsymbol{\rho}, \mathbf{U}) = s_m^i \text{PN}(\boldsymbol{\rho}, \mathbf{U})_m^i - 1 \leq 0 \text{ for } m = 1, 2, \dots, n \\
 \text{variables :} & \quad 0 < x_{min} \leq x_e \leq 1 \text{ for } e = 1, 2, \dots, N_d
 \end{aligned} \tag{48}$$

V. Demonstration Examples

The thermoelastic topology optimization formulation described in the previous sections is demonstrated on two example problems. In both cases, the MMA optimizer³³ has been utilized; however, the algorithm has been modified to take more conservative steps sizes to smooth convergence. All methods, including finite element analysis and topology optimization, have been implemented in MATLAB. The von Mises failure criterion is utilized for all stress constraints and the density filter radius is taken as twice the element size.

A. L-Bracket

The L-shaped bracket is a popular test example for topology optimization with stress criteria in the literature. This is because the design domain contains a re-entrant corner that causes an initial stress singularity that is not removed when the problem is solved using the typical minimum compliance solution strategy. This problem is used here to demonstrate the effectiveness of the stress-constrained formulation with scaled stress aggregation. It should be noted that for a stress-based topology optimization to be considered successful, the maximum stress in the structure should remain at or below a prescribed limit that is based on realistic failure criteria.

The design domain for the L-bracket is given in Figure 5. The structure is fixed in all degrees of freedom along its top edge and a 750 N concentrated load is applied as indicated. To prevent an unresolvable stress singularity that would impede the optimization due to the point load, a 2 by 3 region of elements are taken as non-designable and excluded from the stress constraints. The thickness of the structure is assumed to be 1 mm and the material properties are taken as those of 7075-T6 aluminum (shown in Table 2) at room temperature. The domain is discretized using 6400 quadrilateral plane stress finite elements. The minimum material, stress-constrained topology optimization problem is solved according to the statement in Equation (47) with a total of $n = 10$ stress aggregation regions and the penalization parameter in the p -norm functions is taken as $p = 8$. In the first set of results (at room temperature) that follow, both the SIMP and RAMP interpolation schemes are utilized, with $p_E = 3$ and $R_E = 8$, respectively, and all design variables are initialized with value of 0.5.

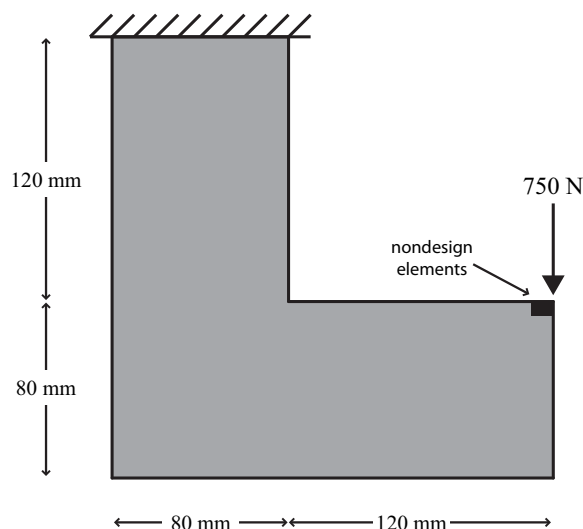


Figure 5. Design domain, boundary conditions, and loading for the L-bracket example problem.

Table 2. Material Properties of 7075-T6 Aluminum³⁴.

Elastic Modulus, E_o (GPa)	68.9
Poisson's Ratio, ν	0.33
Coefficient of Thermal Expansion, α_o ($10^{-6}/^{\circ}\text{C}$)	23.5
Yield Strength, \bar{F} (MPa)	275.0

1. Room Temperature

Figure 6 gives the topology optimization results for the L-shaped bracket with only mechanical loading (room temperature) using both the SIMP and RAMP stiffness interpolations. We observe in the density distributions in Figures 6a and 6b that topologically similar designs are obtained; however, the RAMP design utilizes nearly 6% more material. It is also apparent that not all of the intermediate density material is removed using RAMP and trace amounts of gray material remain. This creates higher stresses in these regions when compared to the surrounding void material since the relaxation on element stresses only effectively zeros the stresses for nearly zero density. We presume this feature is a result of the fundamental difference between the SIMP and RAMP schemes. Recalling that a limitation

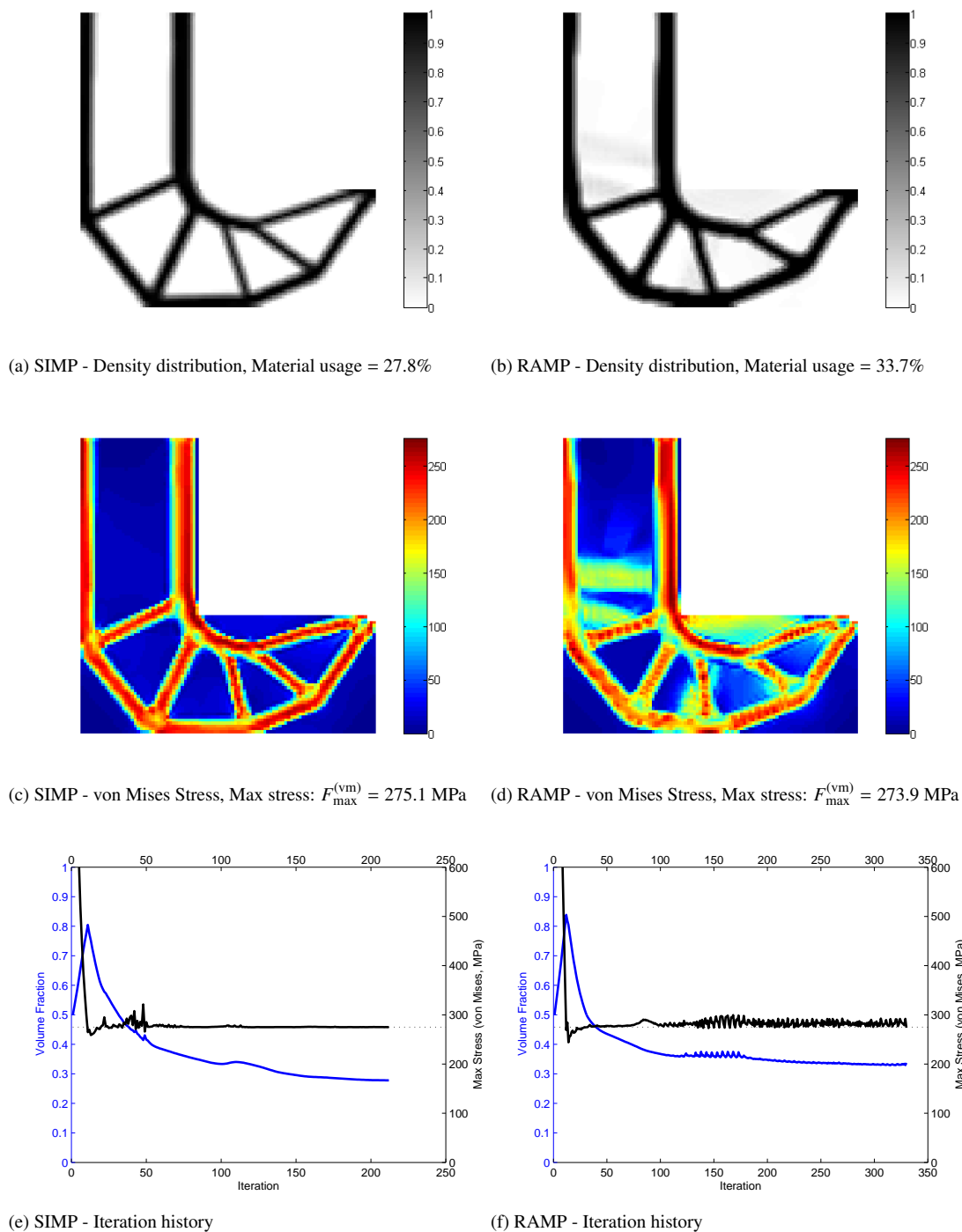


Figure 6. Topology optimization results for the L-shaped bracket with *only mechanical loading* for both (a,c,e) SIMP and (b,d,f) RAMP interpolation on stiffness. (a,b) Density distributions, (c,d) von Mises Stress in MPa, and (e,f) Iteration history for material usage and maximum stress.

of the SIMP interpolation is that it has zero sensitivity at zero density, which RAMP does not. Thus, as material is removed and becomes void, it is much more difficult for it to reappear when utilizing SIMP than RAMP (which is a critical drawback of SIMP for design-dependent loading). When combined with the scaled stress measure, which imparts a small perturbation on the mathematical optimization problem every iteration, the relative insensitivity of SIMP proves to be an advantage. In the RAMP interpolation, the increased sensitivity of responses in low density regions means that the optimization algorithm reacts more strongly to the perturbed problem. This conclusion is supported by the iteration history plots in Figures in 6e and 6f. Compared to the SIMP convergence, considerably more oscillation is evident in the maximum stress convergence when using RAMP, which results from a stronger response to the stress scaling process. The most important observation from this problem is found in Figures 6c and 6d where we note that the maximum stress limit of $\bar{F} = 275.0$ MPa is satisfied. This indicates the scaled stress technique is successful using both SIMP and RAMP in this problem.

2. Thermal Loading

To investigate the effectiveness of the scaled stress measure in the presence of thermal loading, the L-shaped bracket is now subjected to a uniform elevated temperature of $T = 20^\circ\text{C}$. The applied mechanical load of 750 N and boundary conditions remain unchanged. Physically, 20°C does not appear to be a significant source of thermal loading; however, considering the two-dimensional context of the problem, where all strain energy is contained in only in-plane degrees-of-freedom, it actually represents a considerable load. To demonstrate this, the optimal design obtained using the RAMP interpolation scheme, previously shown in Figure 6b, is subjected to the new combined loading environment. The resulting stress distribution is shown in Figure 7. In the figure, all regions that appear as deep red exceed the previous allowable stress of 275.0 MPa and the maximum stress in the domain is now 346.8 MPa, which represents an increase of approximately 25%. We note that the elevated stresses occur directly within the connecting structural members. This implies that while such a material layout carries mechanically-induced stresses very well, it may not be appropriate when additional thermal effects are considered.

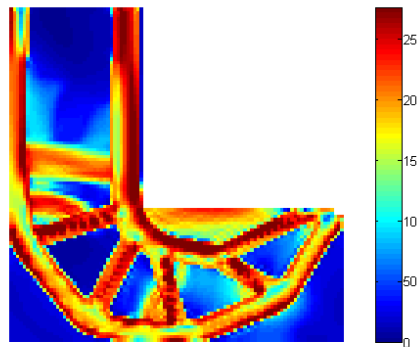


Figure 7. von Mises stress distribution for the design previously shown in Figure 6b subjected to combined thermal and mechanical loading (stress in MPa).

We now incorporate the combined thermal loading and re-solve the topology optimization problem. The RAMP interpolation scheme is utilized here despite the superior performance of the SIMP scheme in the last section with purely mechanical loads because SIMP is not generally effective in the presence of design-dependent loading. The RAMP penalization parameters are taken as $R_E = 8$ for stiffness and $R_\beta = 0$ for the thermal load. The resulting density and stress distributions are given in Figure 8a and the iteration history for volume usage and maximum stress are shown in Figure 8c.

In Figure 8a, we note that a different topological layout is obtained when the effects of the elevated temperature are considered. In this layout, as evidenced by reduced thermal stresses, the material has been redistributed such that structural members do not restrain the thermal expansion of one another. Thus, the stress limit of 275 MPa is satisfied within the tolerances of the optimizer and a nearly identical amount of material has been utilized as the purely mechanical load case. Investigating the iteration history in Figure 8c, the absence of gray material and significant oscillations in convergence compared to previous results in Figure 6f is readily evident. This is attributed to the

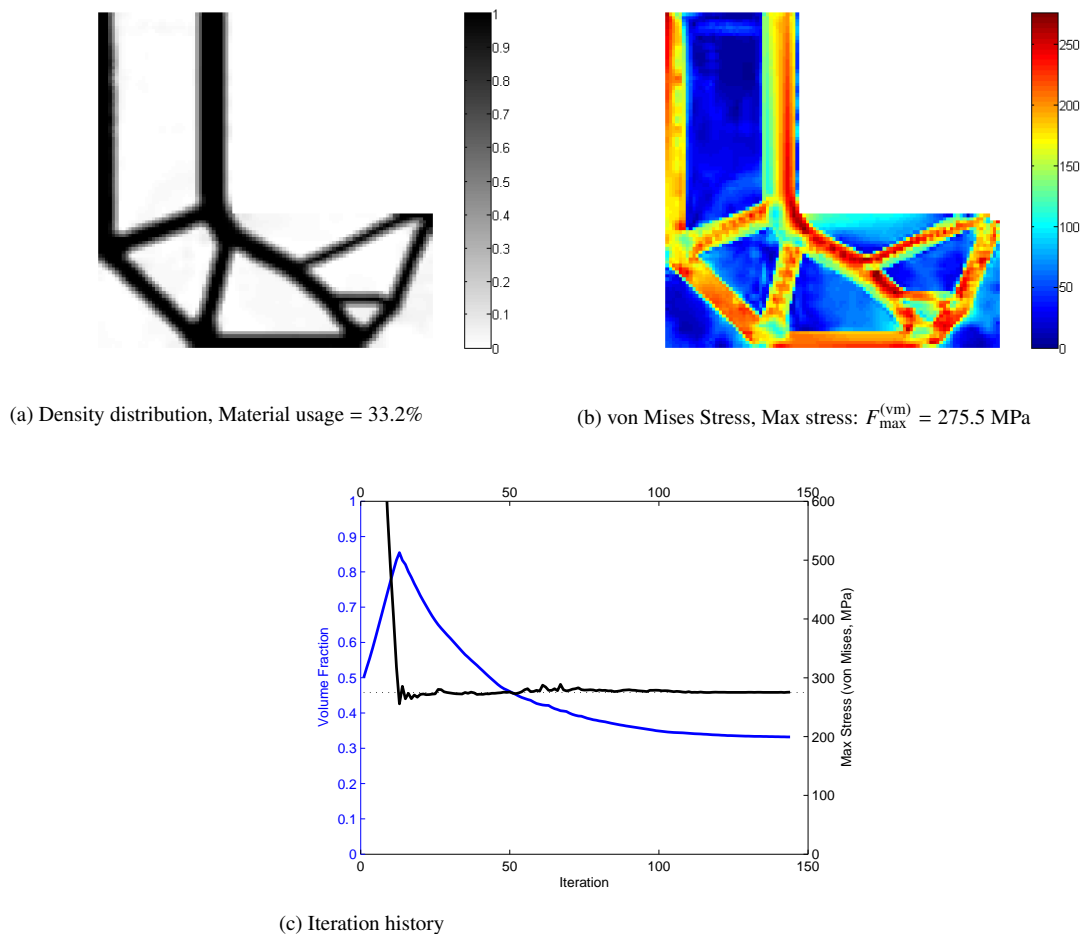


Figure 8. Topology optimization results for the L-shaped bracket with *combined thermal and mechanical loading*. (a) Density distribution, (b) von Mises Stress in MPa, and (c) Iteration history for material usage and maximum stress.

presence of the thermal loading, which due to its design-dependency, serves as a penalty on the reappearance of material. This effectively damps the optimizer's reaction to the scaling stress measures between each iteration.

3. Effectiveness of Scaled Stress Measure

To demonstrate the effectiveness of the scaled stress measure in enforcing local limits on maximum stress, even in the presence of thermal loads, the iteration history of the components used to compute it are shown in Figures 9a and 9b. The results correspond to the designs in Figures 6b (mechanical load only) and 8a (combined thermal and mechanical load), respectively. In the optimization problem, we recall that 10 constraints were utilized based on 10 aggregated regions; however, for demonstration, only results of the first constraint g_1 are shown. In the figure, the blue curve denotes the value of PN_1^i directly computed from the elements in its region according to Equation (26). The red dots denote the actual maximum value of the stress failure criteria (normalized by the limit \bar{F}) within region 1 in each iteration. The green curve denotes the scaling parameter s_1^i that is computed at each iteration using the value of PN_1^{i-1} and the maximum value from the previous iteration as stated in Equation (29). The black curve then gives the product $s_1^i PN_1^i$, which is the scaled aggregation measure that approximately gives the maximum stress value in the region. This quantity is then constrained to limit maximum stresses according to Equation (28). We observe in both cases, the approximation of the maximum value within the region rapidly approaches the actual maximum value within only a small number of iterations and local limits on stress are enforced effectively.

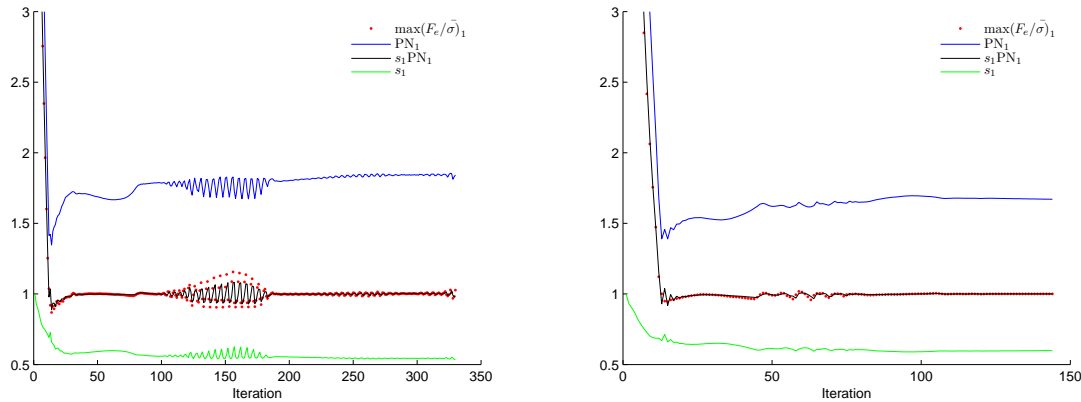


Figure 9. Iteration history for components of scaled stress measure in constraint 1 for (a) room temperature design and (b) combined mechanical and thermal load design.

B. Bi-clamped Thermoelastic Domain

The bi-clamped beam problem is a demonstration example that has been used in a limited number of publications regarding thermoelastic topology optimization to demonstrate the behavior of the compliance objective in the presence of thermal loading. It was first introduced by Rodrigues and Fernandes in 1995⁵. We note that this objective is not likely to yield a useable solution for general thermoelastic problems and the bi-clamped problem is an exception. In this section, we apply the stress-based formulations to investigate their behavior on a simple problem with combined thermal and mechanical loading. In addition, the conventional minimum compliance problem is solved for comparison since, in this case, the formulation is able to produce solutions. Figure 10 shows the design domain for the structure. It is discretized with four node bi-linear quadrilateral plane stress elements with 60 elements in the horizontal direction and 40 elements in the vertical direction. Black areas in the figure denote non-design regions in the model while gray areas give the designable domain. A mechanical load of $F = 150$ kN is applied to the center of the bottom edge along with a uniform temperature increase of $\Delta T = 25^\circ\text{C}$. Similar to the L-shaped bracket example, this temperature level does not seem considerable, but considering the 2D nature of the problem, it in fact represents a significant amount of thermally induced strain energy in the structure. A small non-design region near the application of the mechanical point load is included to prevent a geometrical stress singularity. The material properties are taken as those of 4340 steel at room temperature and are given in Table 3 and a thickness of 1 cm is assumed.

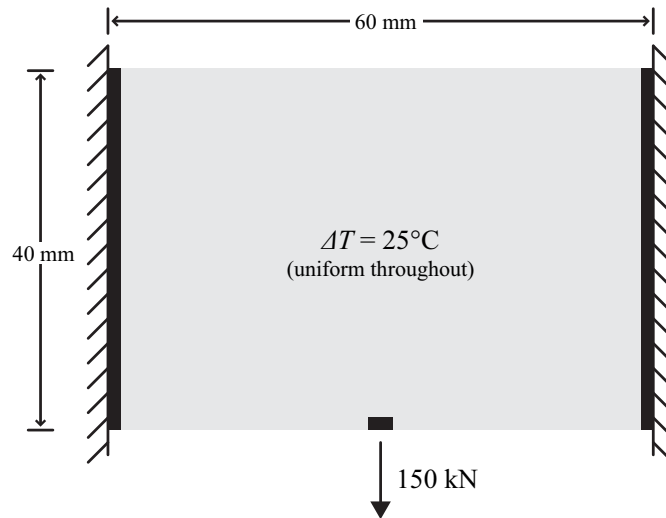


Figure 10. Bi-clamped structural domain with non-design (black) and designable (gray) regions.

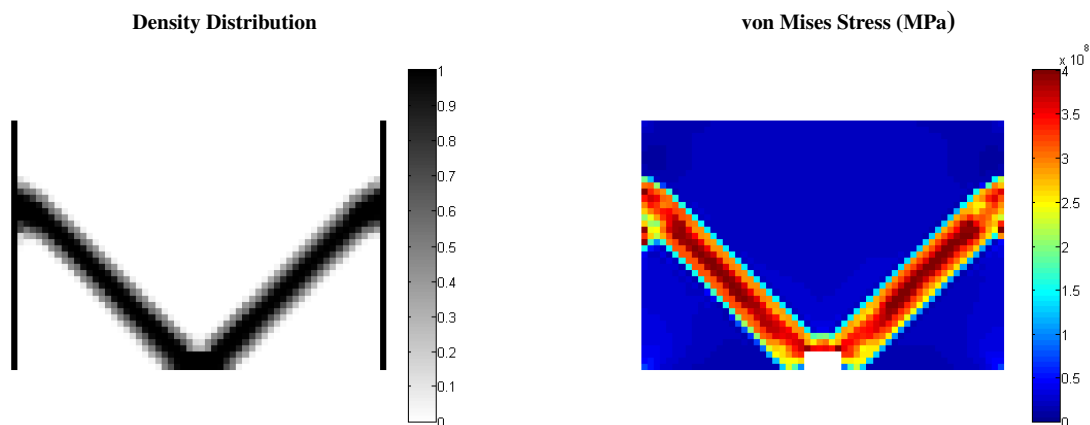
Table 3. Material Properties of 4340 Steel³⁴.

Elastic Modulus, E_o (GPa)	210.0
Poisson's Ratio, ν	0.3
Coefficient of Thermal Expansion, α_o ($10^{-6}/^{\circ}\text{C}$)	11.0
Limit Strength, \bar{F} (MPa)	400.0

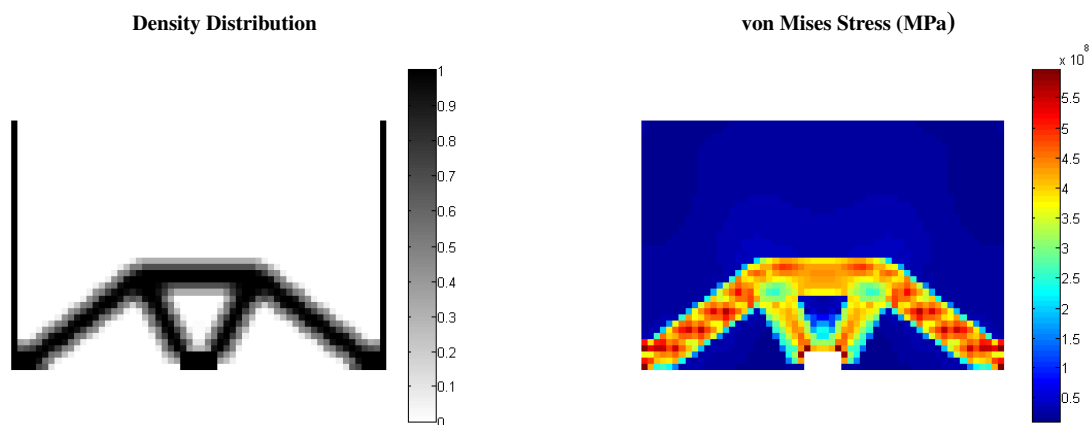
Three different topology optimization problems are solved using the bi-clamped beam domain. First, the minimum volume, stress-constrained problem is solved as stated in Equation (47) using $m = 10$ stress regions on the von Mises failure criterion. The p -norm parameter in the aggregated stress measures is taken as $p = 8$. After obtaining the stress-constrained design, another optimization is performed using the standard minimum compliance, volume constrained formulation in Equation (46) where the volume limit is taken as the volume achieved in the stress-constrained problem. Finally, the minimum compliance problem with volume and stress constraints stated in Equation (48) is solved using the constraint limits from the previous problems. In each formulation, the RAMP interpolation model is utilized with a penalization parameter of $R_E = 8$ on the material stiffness and $R_\beta = 0$.

Figure 11 shows the density and stress distributions and Figure 12 gives the iteration history for topology optimization of the bi-clamped domain with each of the three formulations.

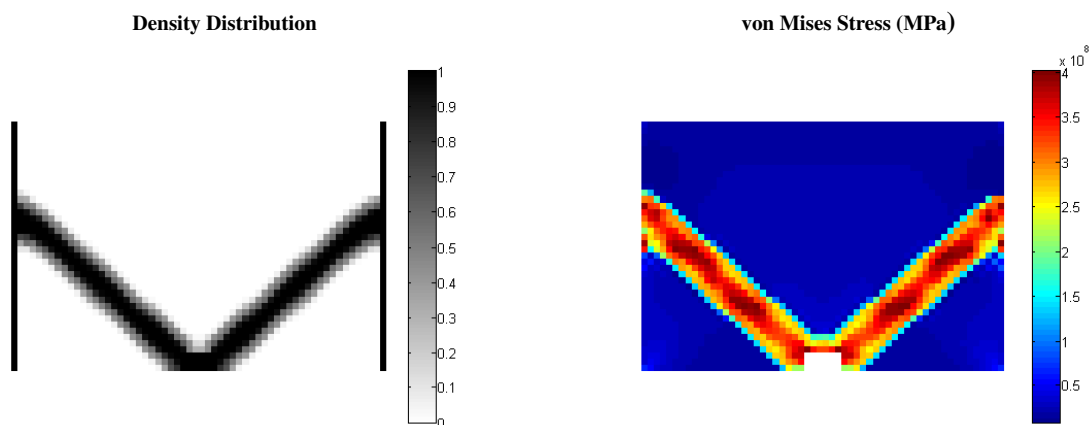
Inspecting results of the stress-constrained problem in Figure 11a, we observe that the stress limit of 400 MPa is satisfied with a material usage of only 14.6%. In addition, the structure is uniformly stressed, which implies it is an effective layout for carrying the combined thermal and mechanical loading. In Figure 11b, we see that a significantly different topology is obtained using the minimum compliance formulation even when the material usage is restricted to near that of the stress-constrained design (15%). A nonuniform stress distribution is also readily evident with significantly higher stresses (note the plots do not use the same color scale in Figure 11). In fact, the maximum stress observed in the minimum compliance design is 596.6 MPa, or nearly a 50% increase, compared to the stress-constrained structure. The areas of greatest stress occur adjacent to the non-design elements near the applied loading and at the lower left and right corners, which from a mechanical design perspective, are expected locations. These comparatively increased stresses are likely due in large part to the internal deformation caused by thermal expansion. Compared to the stress-constrained design, where no structural member lies in an orientation directly between the restrained boundaries and expansion can occur with limited bending deformation in the direction of the applied load, expansion in the minimum compliance design is more restrained. This restraint translates into significant internal thermal loading and increased stress levels that cannot be addressed by simply minimizing compliance. This is supported by the results in Figure 11c, where the stress constraints have been introduced to the minimum compliance problem. In this formulation, results are effectively identical to the purely stress-constrained design, because stress information, which with design-dependent types of loads is not consistent with compliance as with mechanical loading, is directly available to the design optimization problem.



Minimum Volume, Stress-constrained Design: $V_f = 0.146$, $F_{max} = 400.5$ MPa, $c = 315.4$ N · m



Minimum Compliance, Volume Constrained Design: $V_f = 0.15$, $F_{max} = 596.6$ MPa, $c = 310.5$ N · m



Minimum Compliance, Volume and Stress-constrained Design: $V_f = 0.144$, $F_{max} = 400.5$ MPa, $c = 311.4$ N · m

Figure 11. Density and stress distributions for bi-clamped domain topology optimization with (a) stress-constrained formulation, (b) minimum compliance formulation, and (c) minimum compliance formulation with stress constraints.

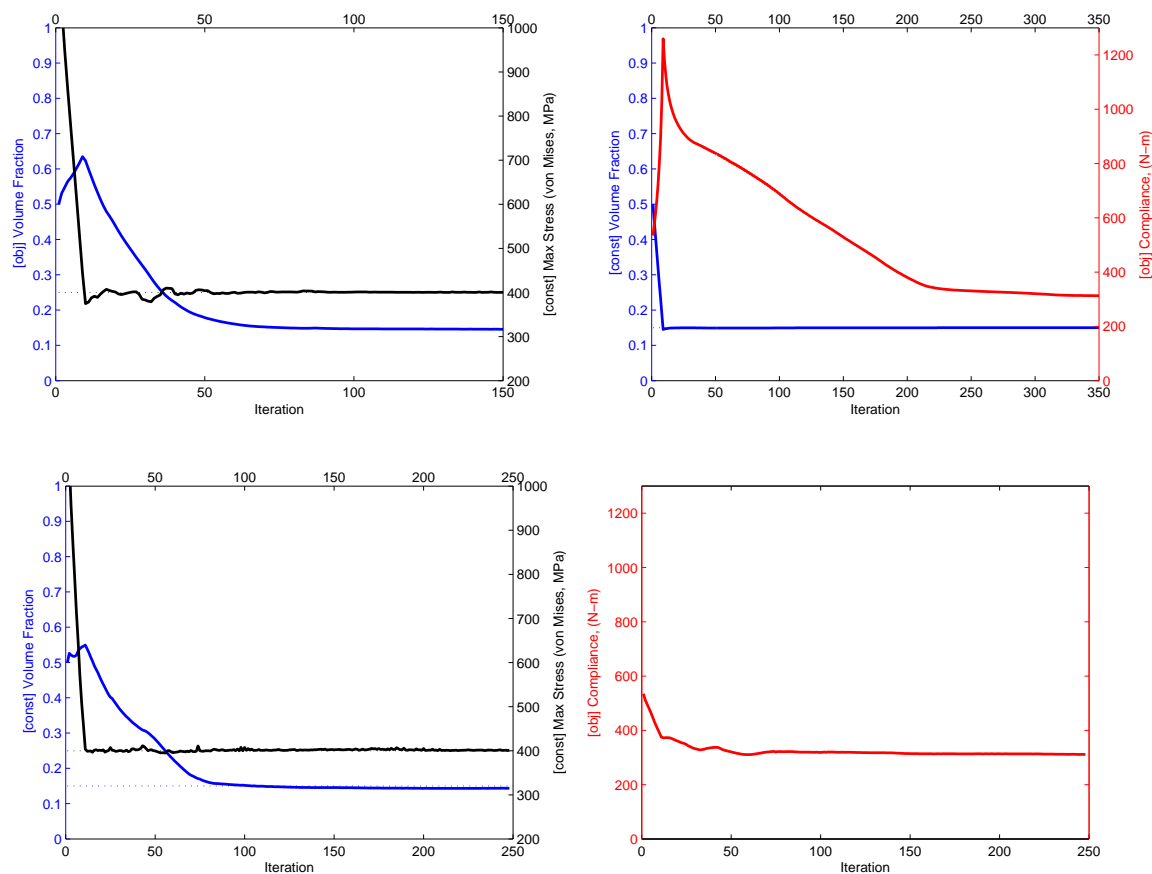


Figure 12. Iteration history for bi-clamped domain topology optimization with (a) stress-constrained formulation, (b) minimum compliance formulation, and (c) minimum compliance formulation with stress constraints.

1. Effectiveness of Scaled Stress Measure

To reaffirm the effectiveness of the scaled stress measure, its components are plotted for the stress constraint corresponding to region 1 in Figure 13. Similar to the L-shaped bracket problem in Section 3, the blue curve denotes the value of PN_1^i computed from the elements in its region according to Equation (26). The red dots give the maximum value of the stress failure criteria (normalized by the limit $\bar{\sigma}$) within region 1 in each iteration. The green curve denotes the scaling parameter s_1^i that is computed at each iteration using the value of PN_1^{i-1} and the maximum value from the previous iteration as stated in Equation (29). The black curve then gives the product $s_1^i PN_1^i$, which is the scaled aggregation measure that approximately gives the maximum stress value in the region. This quantity is then constrained to limit maximum stresses according to Equation (28). Just as in the previous problem, the approximation of the maximum value within the region quickly reaches the actual maximum value within only a small number of iterations and the local stress limits are satisfied.

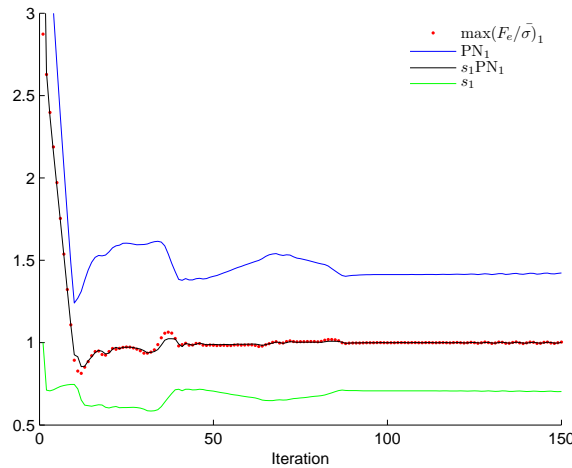


Figure 13. Iteration history for scaled stress measure used in constraint 1 in bi-clamped domain topology optimization.

VI. Conclusions

In this paper we have introduced a topology optimization formulation that can efficiently handle stress constraints in a thermoelastic environment. This development was motivated in part by the lack of such a capability in the structural topology optimization field as well as the need for more advanced design techniques for thermal structures in the aerospace industry, including embedded engine aircraft exhaust structures and hypersonic flight applications. Using a consistent finite element parameterization, which incorporates design-dependent thermoelastic effects, and a scaled aggregation technique for elemental stresses, the process was shown to efficiently enforce maximum stress limits on benchmark numerical examples. In addition, results indicate that by utilizing the stress-based formulation, structural configurations can be obtained with superior thermal stress performance when compared to those from the conventional minimum compliance formulation. A valuable continuation of this work would be to expand the structural optimization to include the effects heat transfer. This will require a coupled analysis procedure to capture the design dependency of heat transfer, which can include combinations of conduction, convection, and radiation, on the topological configuration.

Acknowledgments

The authors would like to acknowledge the support provided by the Air Force Research Laboratory through contract, FA8650-09-2-3938, the Collaborative Center for Multidisciplinary Sciences. The views and conclusions contained herein are those of the authors and should not be interpreted as necessarily representing official policies or endorsements, either expressed or implied, of the Air Force Research Laboratory or the U.S. Government.

References

- ¹M. P. Bendsøe and O. Sigmund, *Topology Optimization: Theory, Methods and Applications*. Springer, 2nd ed., 2003.
- ²J. D. Deaton and R. V. Grandhi, "A survey of structural and multidisciplinary continuum topology optimization: post 2000," *Structural and Multidisciplinary Optimization*, vol. 49, pp. 1–38, January 2014.
- ³M. A. Haney and R. V. Grandhi, "Consequences of Material Addition for a Beam Strip in a Thermal Environment," *AIAA Journal*, vol. 47, pp. 1026–1034, April 2009.
- ⁴J. D. Deaton and R. V. Grandhi, "Significance of Geometric Nonlinearity in the Design of Thermally Loaded Structures," *AIAA Journal of Aircraft*, 2014. (accepted for publication).
- ⁵H. Rodrigues and P. Fernandes, "A material based model for topology optimization of thermoelastic structures," *International Journal for Numerical Methods in Engineering*, vol. 38, no. 12, pp. 1951–1965, 1995.
- ⁶Q. Li, G. P. Steven, and Y. Xie, "Displacement minimization of thermoelastic structures by evolutionary thickness design," *Computer Methods in Applied Mechanics and Engineering*, vol. 179, no. 3–4, pp. 361–378, 1999.
- ⁷Q. Li, G. P. Steven, and Y. M. Xie, "Thermoelastic Topology Optimization for Problems with Varying Temperature Fields," *Journal of Thermal Stresses*, vol. 24, no. 4, pp. 347–366, 2001.
- ⁸W.-Y. Kim, R. V. Grandhi, and M. A. Haney, "Multiobjective Evolutionary Structural Optimization Using Combined Static/Dynamic Control Parameters," *AIAA Journal*, vol. 44, pp. 794–802, April 2006.
- ⁹R. C. Penmetsa, R. V. Grandhi, and M. Haney, "Topology Optimization for an Evolutionary Design of a Thermal Protection System," *AIAA Journal*, vol. 44, pp. 2663–2671, 2006.
- ¹⁰O. Sigmund and S. Torquato, "Design of materials with extreme thermal expansion using a three-phase topology optimization method," *Journal of the Mechanics and Physics of Solids*, vol. 45, no. 6, pp. 1037–1067, 1997.
- ¹¹O. Sigmund, "Design of multiphysics actuators using topology optimization - Part I: One-material structures," *Computer Methods in Applied Mechanics and Engineering*, vol. 190, no. 49–50, pp. 6577–6604, 2001.
- ¹²O. Sigmund, "Design of multiphysics actuators using topology optimization - Part II: Two-material structures," *Computer Methods in Applied Mechanics and Engineering*, vol. 190, no. 49–50, pp. 6605–6627, 2001.
- ¹³C. Jog, "Distributed-parameter optimization and topology design for non-linear thermoelasticity," *Computer Methods in Applied Mechanics and Engineering*, vol. 132, no. 1–2, pp. 117–134, 1996.
- ¹⁴T. Gao and W. Zhang, "Topology optimization involving thermo-elastic stress loads," *Structural and Multidisciplinary Optimization*, vol. 42, no. 5, pp. 725–738, 2010.
- ¹⁵Q. Xia and M. Y. Wang, "Topology optimization of thermoelastic structures using level set method," *Computational Mechanics*, vol. 42, no. 6, pp. 837–857, 2008.
- ¹⁶J. Yan, G. Cheng, and L. Liu, "A uniform optimum material based model for concurrent optimization of thermoelastic structures and materials," *International Journal for Simulation and Multidisciplinary Design Optimization*, vol. 2, pp. 259–266, 2008.
- ¹⁷P. Pedersen and N. L. Pedersen, "Strength optimized designs of thermoelastic structures," *Structural and Multidisciplinary Optimization*, vol. 42, no. 5, pp. 681–691, 2010.
- ¹⁸P. Pedersen and N. L. Pedersen, "Interpolation/penalization applied for strength design of 3D thermoelastic structures," *Structural and Multidisciplinary Optimization*, vol. 42, no. 6, pp. 773–786, 2012.
- ¹⁹J. D. Deaton and R. V. Grandhi, "Stiffening of restrained thermal structures via topology optimization," *Structural and Multidisciplinary Optimization*, vol. 48, no. 4, pp. 731–745, 2013.
- ²⁰B. Wang, J. Yan, and G. Cheng, "Optimal structure design with low thermal directional expansion and high stiffness," *Engineering Optimization*, vol. 43, no. 6, pp. 581–595, 2011.
- ²¹C. Le, J. Norato, T. E. Bruns, C. Ha, and D. A. Tortorelli, "Stress-based topology optimization for continua," *Structural and Multidisciplinary Optimization*, vol. 41, no. 4, pp. 605–620, 2010.
- ²²P. Duysinx and M. P. Bendsøe, "Topology optimization of continuum structures with local stress constraints," *International Journal for Numerical Methods in Engineering*, vol. 43, no. 8, pp. 1453–1478, 1998.
- ²³J. Pereira, E. Fancello, and C. Barcellos, "Topology optimization of continuum structures with material failure constraints," *Structural and Multidisciplinary Optimization*, vol. 26, no. 1–2, pp. 50–66, 2004.
- ²⁴M. Bruggi and P. Venini, "A mixed FEM approach to stress-constrained topology optimization," *International Journal for Numerical Methods in Engineering*, vol. 73, no. 12, pp. 1693–1714, 2008.
- ²⁵M. Bruggi, "On an alternative approach to stress constraints relaxation in topology optimization," *Structural and Multidisciplinary Optimization*, vol. 36, no. 2, pp. 125–141, 2008.
- ²⁶C. E. M. Guilherme and J. S. O. Fonseca, "Topology optimization of continuum structures with epsilon-relaxed stress constraints," in *International Symposium on Solid Mechanics* (M. Alves and H. da Costa Mattos, eds.), vol. 1 of *Mechanics of Solids in Brazil*, pp. 239–250, Brazilian Society of Mechanical Sciences in Engineering, 2007.
- ²⁷J. París, F. Navarrina, I. Colominas, and M. Casteleiro, "Block aggregation of stress constraints in topology optimization of structures," *Advances in Engineering Software*, vol. 41, no. 3, pp. 433–441, 2010.
- ²⁸J. París, F. Navarrina, I. Colominas, and M. Casteleiro, "Improvements in the treatment of stress constraints in structural topology optimization problems," *Journal of Computational and Applied Mathematics*, vol. 234, no. 7, pp. 2231–2238, 2010.
- ²⁹E. Lee, K. A. James, and J. R. A. Martins, "Stress-constrained topology optimization with design-dependent loading," *Structural and Multidisciplinary Optimization*, vol. 46, no. 5, pp. 647–661, 2012.
- ³⁰E. Holmberg, B. Torstenfelt, and A. Klarbring, "Stress constrained topology optimization," *Structural and Multidisciplinary Optimization*, vol. 48, no. 1, pp. 33–47, 2013.
- ³¹O. Sigmund and K. Maute, "Topology optimization approaches," *Structural and Multidisciplinary Optimization*, vol. 48, no. 6, pp. 1031–1055, 2013.

³²T. E. Bruns and D. A. Tortorelli, "Topology optimization of non-linear elastic structures and compliant mechanisms," *Computer Methods in Applied Mechanics and Engineering*, vol. 190, no. 26-27, pp. 3443–3459, 2001.

³³K. Svanberg, "The method of moving asymptotes - a new method for structural optimization," *International Journal for Numerical Methods in Engineering*, vol. 24, no. 2, pp. 359–373, 1987.

³⁴"Metallic Materials and Elements for Aerospace Vehicle Structures," Tech. Rep. MIL-HDBK-5H, U.S. Department of Defense, 1998.